

Cite this: *Nanoscale*, 2015, 7, 17261Received 19th August 2015,
Accepted 23rd September 2015

DOI: 10.1039/c5nr05631d

www.rsc.org/nanoscale

Boosting the sensitivity of Nd³⁺-based luminescent nanothermometers†

Sangeetha Balabhadra,^{a,b} Mengistie L. Debasu,^a Carlos D. S. Brites,^a
Luís A. O. Nunes,^c Oscar L. Malta,^d João Rocha,^b Marco Bettinelli^e and
Luís D. Carlos^{*a}

Luminescence thermal sensing and deep-tissue imaging using nanomaterials operating within the first biological window (ca. 700–980 nm) are of great interest, prompted by the ever-growing demands in the fields of nanotechnology and nanomedicine. Here, we show that (Gd_{1-x}Nd_x)₂O₃ (x = 0.009, 0.024 and 0.049) nanorods exhibit one of the highest thermal sensitivity and temperature uncertainty reported so far (1.75 ± 0.04% K⁻¹ and 0.14 ± 0.05 K, respectively) for a nanothermometer operating in the first transparent near infrared window at temperatures in the physiological range. This sensitivity value is achieved using a common R928 photomultiplier tube that allows defining the thermometric parameter as the integrated intensity ratio between the ⁴F_{5/2} → ⁴I_{9/2} and ⁴F_{3/2} → ⁴I_{9/2} transitions (with an energy difference between the barycentres of the two transitions >1000 cm⁻¹). Moreover, the measured sensitivity is one order of magnitude higher than the values reported so far for Nd³⁺-based nanothermometers enlarging, therefore, the potential of using Nd³⁺ ions in luminescence thermal sensing and deep-tissue imaging.

Introduction

The accurate measurement of temperature is crucial across a broad spectrum of areas, including scientific research, consumer electronics, industrial manufacturing and monitoring processes (namely in automotive, petrochemical, aerospace and defence industries), health, and safety.^{1–3} The emerging appli-

cations of temperature sensors in microelectronics, nanotechnology and nanomedicine have fuelled the demand with recent advances in accurate, noninvasive, self-referenced and high-resolution temperature measurement at the submicrometer scale.^{4–11} Indeed, although contact thermometers (such as thermocouples and thermistors) represent the major share of the present market, they require a thermal connection that disturbs the measurements in small systems being, in general, unsuitable for scales below 10 μm.^{5,9} Furthermore, conventional thermometers require an electrical link in the sensor system that hamper their applications in conditions where electromagnetic noise is strong, sparks are hazardous and the environment is corrosive.¹²

Recent years have witnessed an enormous development in the design of distinct phosphors based on organic dyes,¹² polymers,¹³ semiconductor nanocrystals,¹⁴ and trivalent lanthanide (Ln³⁺) ions^{1,2,5,15–20} as luminescence temperature sensors. The latter are among the most versatile thermal probes used in luminescent nanothermometry. In particular, because Nd³⁺ has a ladder-like intra-4f energy-level structure the excitation and emission lie within the first biological window (700–980 nm) where the transparency of living tissues is high due to low optical absorption, offering much potential for deep-tissue luminescence imaging²⁵ and temperature sensing.²¹ Only a handful of reports on luminescent thermometry involving Nd³⁺-doped nanocrystals are available, including LaF₃:Nd³⁺,^{21–23} NaYF₄:Nd³⁺,²⁴ and yttrium aluminium garnet (YAG):Nd³⁺.²⁵ The recent example by Jaque's group combining NaGdF₄:Nd³⁺ nanoparticles and PbS/CdS/ZnS quantum dots in a single-encapsulated organic-inorganic hybrid nanostructure operating in the second biological window (1000–1350 nm) between 283 and 328 K (ref. 26) is not discussed here as the Nd³⁺ emission at 1060 nm is temperature independent.

In all of the abovementioned examples in which the Nd³⁺ emission is temperature dependent,^{21–25} the intensity ratio between the ⁴F_{3/2(1)} → ⁴I_{9/2} and ⁴F_{3/2(2)} → ⁴I_{9/2} transitions (where ⁴F_{3/2(1)} and ⁴F_{3/2(2)} are two Stark components of the ⁴F_{3/2} multiplet) is used as the ratiometric temperature parameter.

^aDepartment of Physics and CICECO Aveiro Institute of Materials, University of Aveiro, 3810-193 Aveiro, Portugal. E-mail: lcarlos@ua.pt

^bDepartment of Chemistry and CICECO Aveiro Institute of Materials, University of Aveiro, 3810-193 Aveiro, Portugal

^cInstituto de Física de São Carlos, Universidade de São Paulo - USP, CEP 13560-970, São Carlos, SP, Brazil

^dDepartamento de Química Fundamental-CCEN-UFPE, Cidade Universitária, Recife, PE 50670-901, Brazil

^eLuminescent Materials Laboratory, Department of Biotechnology, University of Verona, 37134 Verona, Italy

†Electronic supplementary information (ESI) available. See DOI: 10.1039/c5nr05631d

Table 1 Excitation wavelength, λ_{exc} , temperature range, ΔT , maximum relative sensitivity, S_m , and temperature for which it occurs, T_m , of Nd^{3+} -based thermometers

	Host	λ_{exc} (nm)	Transitions	ΔT (K)	S_m (% K^{-1})	T_m (K)	Detector
Nanoparticles	Gd_2O_3	580	$^4\text{F}_{5/2}, ^4\text{F}_{3/2} \rightarrow ^4\text{I}_{9/2}$	288–323	1.75	288	R928 PMT
	YAG^{23}	808	$^4\text{F}_{3/2}$ (Stark levels)	283–343	0.15	283	Silicon based CCD
	NaYF_4^{24}	830	$^4\text{F}_{3/2}$ (Stark levels)	273–423	0.12	273	Raman microscope
	LaF_3^{22}	808	$^4\text{F}_{3/2}$ (Stark levels)	283–333	0.10	283	Silicon based CCD
Microcrystals	NaYF_4^{42}	793.8	$^4\text{F}_{5/2}, ^4\text{F}_{3/2} \rightarrow ^4\text{I}_{9/2}$	323–673	0.58	500	R928 PMT
		864.2	$^4\text{F}_{7/2}, ^4\text{F}_{5/2} \rightarrow ^4\text{I}_{9/2}$		0.55	500	
		574.8	$^4\text{F}_{7/2}, ^4\text{F}_{3/2} \rightarrow ^4\text{I}_{9/2}$		1.12	500	
Bulk powders	CaWO_4^{43}	980	$^4\text{F}_{5/2}, ^4\text{F}_{3/2} \rightarrow ^4\text{I}_{9/2}$	303–873	0.27	730	PMT-H-S1-CR131
			$^4\text{F}_{7/2}, ^4\text{F}_{3/2} \rightarrow ^4\text{I}_{9/2}$		0.15	1353	
			$^4\text{F}_{7/2}, ^4\text{F}_{5/2} \rightarrow ^4\text{I}_{9/2}$		0.30	668	
			$^4\text{F}_{5/2}, ^4\text{F}_{3/2} \rightarrow ^4\text{I}_{9/2}$		1.10 ^a	358	
	$\text{La}_2\text{O}_2\text{S}^{27}$	532	$^4\text{F}_{5/2}, ^4\text{F}_{3/2} \rightarrow ^4\text{I}_{9/2}$	30–600			Acton ID-441-C InGaAs photodiode

^a Although the authors reported a maximum sensitivity of 1.95% K^{-1} at 270 K, for $T < 350$ K the integrated area of the $^4\text{F}_{5/2} \rightarrow ^4\text{I}_{9/2}$ transition is less than 4% of the $^4\text{F}_{3/2} \rightarrow ^4\text{I}_{9/2}$ one. As below 350 K the error in the base line is ca. 5%, the signal is of the order of magnitude of the noise level.

These thermometers have the inherent limitation of very low relative sensitivity (ca. 0.1% K^{-1} , Table 1) due to the small energy difference between the two Stark components (typically $<100 \text{ cm}^{-1}$). The relative sensitivity may be increased by more than one order of magnitude (e.g., 1.10% K^{-1} at 358 K for $\text{La}_2\text{O}_2\text{S}:\text{Nd}^{3+}$ bulk powder²⁷) if the thermometric parameter is defined as the $^4\text{F}_{5/2} \rightarrow ^4\text{I}_{9/2}$ to $^4\text{F}_{3/2} \rightarrow ^4\text{I}_{9/2}$ intensity ratio (Table 1). Despite this, and as mentioned above, all Nd^{3+} -based nanothermometers reported so far use a thermometric parameter defined by the intensity ratio between the $^4\text{F}_{3/2(1)} \rightarrow ^4\text{I}_{9/2}$ and $^4\text{F}_{3/2(2)} \rightarrow ^4\text{I}_{9/2}$ transitions. The type of detectors used for measuring the Nd^{3+} emission in the 800–900 nm range essentially determines that choice. In the works of Wawrzynczyk *et al.*,²⁴ Rocha *et al.*,^{22,23} and Benayas *et al.*,²⁵ a charge-coupled device (CCD) silicon-based detector was used, whose performance is severely compromised for wavelengths between 800 and 850 nm (in these works the experimental apparatus includes filters to avoid the residual laser excitation signal that obscures the $^4\text{F}_{5/2} \rightarrow ^4\text{I}_{9/2}$ transition at 830 nm).

Here, we wish to report a new nanothermometer based on $(\text{Gd}_{0.991}\text{Nd}_{0.009})_2\text{O}_3$ nanorods with maximum temperature relative sensitivity of $1.75 \pm 0.04\% \text{ K}^{-1}$ (at 288 K), one order of magnitude higher than the maximum value (0.15% K^{-1} at 283 K (ref. 25)) reported so far for analogous nanosystems (Table 1). This unprecedented relative sensitivity for Nd^{3+} nanothermometers is achieved using a common R928 photomultiplier to measure the Nd^{3+} emission in the 800–920 nm wavelength range allowing defining the thermometric parameter as the integrated intensity ratio between the $^4\text{F}_{5/2} \rightarrow ^4\text{I}_{9/2}$ and $^4\text{F}_{3/2} \rightarrow ^4\text{I}_{9/2}$ transitions.

Experimental

Materials

Gd_2O_3 (99.9%) and Nd_2O_3 (99.9%) (Jinan Henghua Sci. & Tec. Co., Ltd) were dissolved separately in ultra-pure nitric acid (HNO_3 65%, PA-ISO) in order to obtain the respective lantha-

nide nitrate solutions. Ammonia (NH_3 25 wt%, PA-ISO) was also used during the synthesis. The chemicals were used as they were received without further purification. In all experiments, distilled water was used.

Synthesis

A simple wet-chemical route was used to synthesize $(\text{Gd}_{0.99}\text{Nd}_{0.01})_2\text{O}_3$ nanorods (nominal concentration of 1.00 mol% Nd^{3+} relative to Gd^{3+}), following a previously reported procedure.²⁸ Briefly, aqueous solutions of $\text{Gd}(\text{NO}_3)_3$ (8.91 mL, 0.4 M), and $\text{Nd}(\text{NO}_3)_3$ (0.09 mL, 0.1 M) were mixed with distilled water (40 mL) in a 250 mL-round-bottom flask. Then, an aqueous NH_3 solution (30 mL, 25 wt%) was added dropwise to the above solution under stirring, at room temperature. The resulting white viscous solution was sonicated for about 10 minutes and then vigorously stirred again for additional 10 minutes. In the next step, the solution was heated up to 343 K and maintained at this temperature for 16 h under continuous magnetic stirring. After 16 h, heating and stirring of the reaction were terminated, and the solution was allowed to cool down to room temperature. The white precipitate was collected, centrifuged and washed several times with distilled water and once with ethanol. The resulting precursor was dried at 348 K for 24 h in air, yielding $(\text{Gd},\text{Nd})\text{-(OH)}_3$ nanorod powder, which was finely ground in an agate mortar and pestle. Finally, a few milligrams of this fine powder was calcined at 973 K for 3 h with heating and cooling rates of 2 and 5 K min^{-1} , respectively, affording $(\text{Gd}_{0.99}\text{Nd}_{0.01})_2\text{O}_3$ nanorod powder. The same procedure was followed to obtain $(\text{Gd}_{0.975}\text{Nd}_{0.025})_2\text{O}_3$ and $(\text{Gd}_{0.95}\text{Nd}_{0.05})_2\text{O}_3$ nanorods by changing the relative Gd^{3+} and Nd^{3+} concentrations.

Moreover, the nanorods are quite insensitive to moisture, as the emission spectra measured during one week in laboratory atmosphere displays no significant differences (Fig. S1 in ESI†).

Instrumental

The Nd^{3+} and Gd^{3+} contents in the calcined $(\text{Gd,Nd})_2\text{O}_3$ nanocrystals were determined by inductively coupled plasma optical emission spectroscopy (ICP-OES-Activa-M, Horiba Jobin Yvon). The powder X-ray diffraction patterns of the as-synthesized and calcined powder samples were collected on a PANalytical Empyrean X-ray diffractometer with $\text{CuK}\alpha_1$ radiation, in the 2θ range 10° to 60° in the reflection scanning mode. The reference data were taken from the International Centre for Diffraction Data (ICDD) database. The morphology of the calcined samples was analysed on a Jeol JEM-2200FS transmission electron microscope (TEM) operated at 200 kV and Hitachi SU-70 scanning electron microscopy in the transmission mode (STEM) operated at 30 kV. Photoluminescence spectra were obtained using a dye laser (Coherent-599/Rhodamine 6G) pumped with a Inova 400 Coherent Ar ion laser. The emission was dispersed by a single Monospec 27 Spex monochromator coupled to a R928 (Hamamatsu) photomultiplier. The temperature was varied from 288 to 328 K using a N_2 cryostat equipped with a 320 Auto tuning temperature controller (LakeShore). A modular double grating excitation spectrofluorimeter with a TRIAX 320 emission monochromator (Nanolog, Horiba Scientific) coupled to a Symphony II detector with an InGaAs array was also used to record room-temperature emission spectra between 800 and 1200 nm. The excitation source was a Xe lamp. The emission spectra were corrected for detection and optical spectral response of the spectrofluorimeter. Luminescence decay curves were measured by exciting the samples at 808 nm with an optical parametric oscillator (OPO, Surelite/Continuum SLII-10) pumped by the third harmonic (355 nm) of a Nd-YAG laser (Surelite II/Continuum, 10 Hz, 5 ns) using the Monospec 27 Spex monochromator and the InGaAs detector. A digital oscilloscope (TekTronix/TDS380) was used to register the decay curves.

Results and discussion

The nominal concentrations of 1.00, 2.50 and 5.00 mol% Nd^{3+} relative to Gd^{3+} in the as-synthesised materials were found to be 0.94, 2.43 and 4.91 mol% Nd^{3+} , respectively, in the final $(\text{Gd}_{1-x}\text{Nd}_x)_2\text{O}_3$ nanorods. Fig. 1 shows the powder X-ray diffraction patterns of the as-synthesized $(\text{Gd}_{1-x}\text{Nd}_x)_2\text{O}_3$ ($x = 0.009$, 0.024 and 0.049) nanorods. The samples contain the cubic phase, in agreement with Gd_2O_3 standard structure data listed in the International Centre for Diffraction Data (ICDD) database (04-015-1513) and references.^{16,28} No new reflections or changes in the diffraction peak positions are observed when the amount of Nd^{3+} increases from 1 to 5 mol%, indicating that these ions have been effectively introduced in the Gd_2O_3 host lattice. Transmission electron microscopy images show nanorods roughly uniform in diameter and length (Fig. 2A–C). The measured distances between adjacent planes were determined from these images as 0.314 ± 0.004 nm (222) and 0.275 ± 0.004 nm (400) along with the corresponding orientations of the indexed planes by powder X-ray diffraction (Fig. 2B and C).

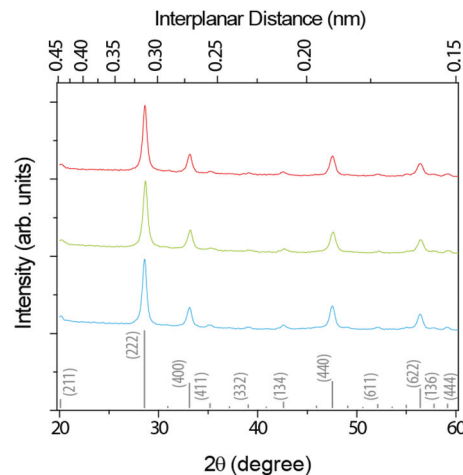


Fig. 1 Powder X-ray diffraction patterns of $(\text{Gd}_{1-x}\text{Nd}_x)_2\text{O}_3$ nanorods, $x = 0.009$ (blue), 0.024 (green) and 0.049 (red). The most intense reflections of cubic Gd_2O_3 are also depicted (ICDD Card no 04-015-1513).

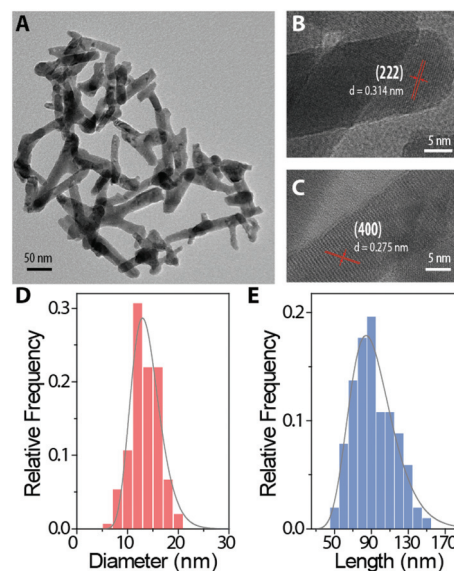


Fig. 2 (A) Transmission electron microscopy image of $(\text{Gd}_{0.991}\text{Nd}_{0.009})_2\text{O}_3$ nanorods. (B and C) (222) and (400) crystallographic planes and interplanar distances of cubic Gd_2O_3 . (D and E) Nanorods size distribution computed from transmission electron microscopy images (over 100 rods measured). The solid lines are the best fit of the experimental data to a log-normal distributions ($r^2 > 0.902$) yielding a diameter of 13.5 ± 3.5 nm and a length of 91.0 ± 11.0 nm.

The values are in accord with the corresponding interplanar distances listed in the ICDD database, 0.3121160 nm and 0.2703000 nm. As shown in Fig. 2D and E, the diameter and the length distributions of the nanorods range, respectively, from 6 to 20 nm and from 50 to 150 nm, with average values of 13.5 ± 3.5 nm and 91.0 ± 11.0 nm.

Fig. 3A shows the emission spectra of $(\text{Gd}_{1-x}\text{Nd}_x)_2\text{O}_3$ nanorods ($x = 0.009$, 0.024 and 0.049) excited at 580 nm and

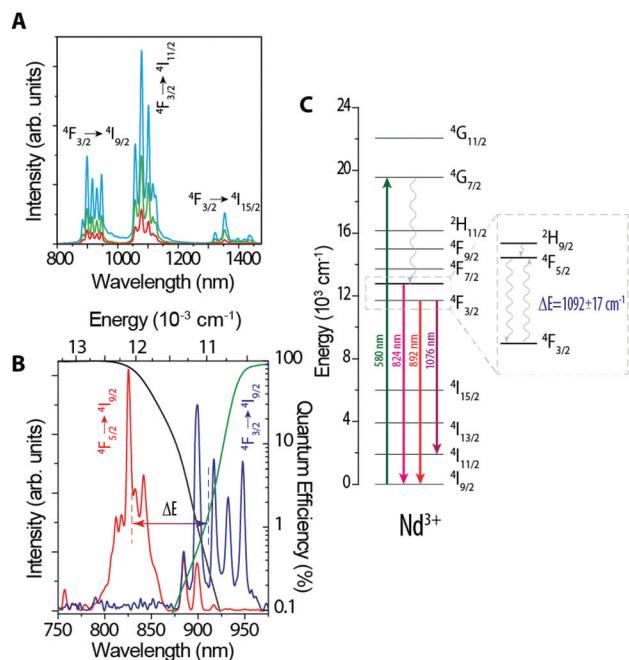


Fig. 3 Room-temperature emission spectra of: (A) $(\text{Gd}_{1-x}\text{Nd}_x)_2\text{O}_3$ nanorods, $x = 0.009$ (blue), 0.024 (green) and 0.049 (red), each spectra was normalized to the corresponding Nd^{3+} ion concentration. (B) $(\text{Gd}_{0.991}\text{Nd}_{0.009})_2\text{O}_3$ in the 750–980 nm range measured with the R928 (red) and InGaAs (blue) detectors. Black and green lines depict, respectively, the photosensitivity of the R928 photomultiplier and InGaAs-based detector. The excitation wavelength is 580 nm. (C) Partial energy-level diagram of Nd^{3+} ions⁴¹ highlighting the absorption at 580 nm and the emissions at 824, 892 and 1076 nm. The expansion depicts the thermally coupled $^4\text{F}_{3/2}$ and $^4\text{F}_{5/2}$ levels.

recorded in the range 800–1200 nm with a InGaAs detector. The spectra were normalized to the corresponding Nd^{3+} concentrations. The energy and relative intensities of the $^4\text{F}_{3/2} \rightarrow ^4\text{I}_{9/2}$ and $^4\text{F}_{3/2} \rightarrow ^4\text{I}_{11/2}$ transitions are independent of the Nd^{3+} molar concentration. Fig. S2 in ESI† shows the semi-logarithmic plot of the experimental decays of the $^4\text{F}_{3/2}$ level for the $(\text{Gd}_{1-x}\text{Nd}_x)_2\text{O}_3$ nanorods ($x = 0.009$, 0.024 and 0.049) obtained at 300 K. As can be seen, the decay curves deviate from a single exponential at short times and the $^4\text{F}_{3/2}$ lifetime shortens with increasing Nd^{3+} concentration, $(0.134 \pm 0.005) \times 10^{-3}$ s, for $x = 0.009$, $(0.060 \pm 0.002) \times 10^{-3}$ s, for $x = 0.024$, and $(0.020 \pm 0.001) \times 10^{-3}$ s, for $x = 0.049$. The $^4\text{F}_{3/2}$ lifetime values correspond to an average value defined by:

$$\langle \tau \rangle = \frac{\int_{t_0}^{t_1} I(t) dt}{\int_{t_0}^{t_1} I(t) dt} \quad (1)$$

where $I(t)$ is the emission intensity at time t , $t_0 = 0.05 \times 10^{-3}$ s is the initial delay and t_1 is the time value where the luminescence intensity reaches the background.^{29,30} Cubic Gd_2O_3 contains two crystallographically non-equivalent Nd^{3+} sites with C_2 (noncentrosymmetric) and C_{3i} or S_6 (centrosymmetric) local symmetries in a 3 : 1 occupation ratio.²⁸ However, as the $^4\text{F}_{3/2} \rightarrow ^4\text{I}_{11/2}$ transition is forbidden in C_{3i} or S_6 local sym-

metry, the deviation from a single-exponential character of the $^4\text{F}_{3/2}$ decays, and the reduction of the corresponding lifetime values as concentration increases can be due to Nd^{3+} -to- Nd^{3+} energy transfer that is dominated by cross-relaxation processes, such as $(^4\text{F}_{3/2}, ^4\text{I}_{9/2}) \rightarrow (^4\text{I}_{15/2}, ^4\text{I}_{15/2})$.^{30–33} Multiphonon relaxation is expected to be small because of the energy gap between the $^4\text{F}_{3/2}$ and $^4\text{I}_{15/2}$ levels and the values of the phonon energy involved. Thus, in order to minimize energy losses we have used the low Nd^{3+} concentration $(\text{Gd}_{0.991}\text{Nd}_{0.009})_2\text{O}_3$ sample in all subsequent measurements. Furthermore, the longer lifetime of Nd^{3+} in this sample is preferable for applications in bioimaging due to the potential screening of tissue autofluorescence under visible light excitation, e.g., 580 nm. We further studied the dependence of the $^4\text{F}_{3/2}$ lifetime with temperature for $(\text{Gd}_{0.991}\text{Nd}_{0.009})_2\text{O}_3$ nanorods between 133 and 323 K (Fig. S3 in ESI†). As can be seen, the decay curves deviate from a single exponential and the $^4\text{F}_{3/2}$ lifetime does not show a significant change with the temperature, $(0.143 \pm 0.005) \times 10^{-3}$ s, for 323 K, $(0.141 \pm 0.005) \times 10^{-3}$ s, for 273 K, $(0.140 \pm 0.005) \times 10^{-3}$ s, for 223 K, and $(0.133 \pm 0.005) \times 10^{-3}$ s, for 133 K (the minimal change lies within the error of experimental conditions). Hence $^4\text{F}_{3/2}$ emission decay curves clearly shows that the temperature dependence of the $^4\text{F}_{3/2}$ lifetime is irrelevant for temperatures near 300 K evidencing that these nanorods cannot be used as luminescent temperature sensors based on the emission lifetime near room temperature.

Fig. 3B displays the emission spectrum of $(\text{Gd}_{0.991}\text{Nd}_{0.009})_2\text{O}_3$ in the 725–975 nm range measured with a R928 photomultiplier and an InGaAs-based detector at 580 nm excitation. Due to the detection limit of the latter detector in the 720–850 nm region, the $^4\text{F}_{5/2} \rightarrow ^4\text{I}_{9/2}$ transition (800–850 nm) could not be discerned. In contrast, this transition is clearly seen in the spectrum recorded using the R928 detector. Moreover, as the three more energetic Stark components of the $^4\text{F}_{3/2} \rightarrow ^4\text{I}_{9/2}$ transition are observed in the spectrum measured using the R928 detector (Fig. 3B) this detector may be used to measure the Nd^{3+} emission in the 800–920 nm range. This allows defining the thermometric parameter $\Delta = I_1/I_2$ where I_1 and I_2 are the integrated intensity of the $^4\text{F}_{5/2} \rightarrow ^4\text{I}_{9/2}$ and $^4\text{F}_{3/2} \rightarrow ^4\text{I}_{9/2}$ transitions, respectively. These two transitions are particularly good for thermal sensing because their intensity ratio shows a significant temperature dependence because the experimental energy gap between the barycentre energy of the $^4\text{F}_{5/2}$ and $^4\text{F}_{3/2}$ levels is much larger ($\Delta E = 1092 \pm 17 \text{ cm}^{-1}$, Fig. 3C) than that between two $^4\text{F}_{3/2}$ Stark sublevels ($<100 \text{ cm}^{-1}$). Instead of using the formal definition of barycentre of a J - J' transition we decide to use the fitting envelope of the $^4\text{F}_{5/2} \rightarrow ^4\text{I}_{9/2}$ and $^4\text{F}_{3/2} \rightarrow ^4\text{I}_{9/2}$ transitions due to experimental difficulties in assigning precisely the Stark-Stark transitions (Fig. S4 in ESI†). A good agreement was obtained with the value computed by Carnal *et al.* for $\text{LaF}_3:\text{Nd}^{3+}$ (1039 cm^{-1}).³⁴

The emission spectra of $(\text{Gd}_{0.991}\text{Nd}_{0.009})_2\text{O}_3$ measured with the R928 detector in the 288–323 K (physiological range) at 580 nm excitation, Fig. 4A, shows that increasing the tempera-

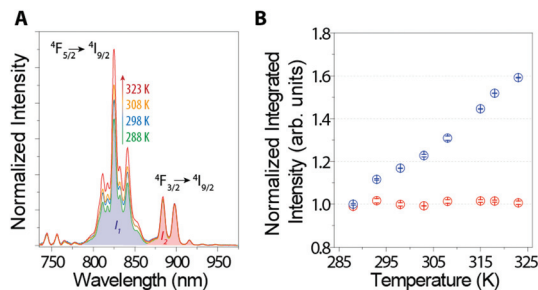


Fig. 4 (A) Emission spectra of $(\text{Gd}_{0.991}\text{Nd}_{0.009})_2\text{O}_3$ nanorods in the 288–323 K range under 580 nm excitation. (B) Normalized integrated intensity of ${}^4\text{F}_{5/2} \rightarrow {}^4\text{I}_{9/2}$ (I_1 , blue) and of ${}^4\text{F}_{3/2} \rightarrow {}^4\text{I}_{9/2}$ (I_2 , red) computed using the 782–865 nm and the 865–925 nm wavelength range, respectively.

ture results in a significant variation in the ratio of intensities of the ${}^4\text{F}_{5/2} \rightarrow {}^4\text{I}_{9/2}$ and ${}^4\text{F}_{3/2} \rightarrow {}^4\text{I}_{9/2}$ transitions: while I_2 is nearly constant, I_1 increases approximately 60% (Fig. 4B). The emission intensity ratio Δ was converted to temperature using the calibration curve represented in Fig. S5 in ESI.† The repeatability of the nanothermometer was measured several times in consecutive temperature cycles of laser irradiation between 288 and 323 K and it was found that Δ is fully reversible without any significant changes, in accord to what was reported for the analogous $(\text{Gd}, \text{Yb}, \text{Er})_2\text{O}_3$ nanothermometers.¹⁶

The thermometric performance is measured by the relative sensitivity S_r :³⁵

$$S_r = \frac{1}{\Delta} \frac{\partial \Delta}{\partial T} \quad (2)$$

which is the figure of merit normally used to compare thermometers, irrespective of their nature.¹ Fig. 5A depicts the temperature dependence of the relative sensitivity of $(\text{Gd}_{0.991}\text{Nd}_{0.009})_2\text{O}_3$ nanorods. The maximum relative sensitivity value of $1.75 \pm 0.04\% \text{ K}^{-1}$ attained at 288 K is, to the best

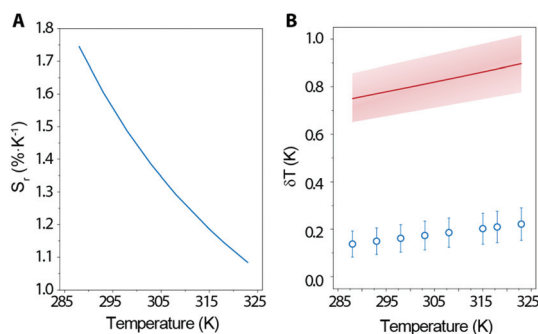


Fig. 5 (A) Relative sensitivity of the thermometer decreasing from 1.75 ± 0.04 to $1.08 \pm 0.03\% \text{ K}^{-1}$ in the 288–323 K. (B) Temperature uncertainty computed using eqn (3) (open points) and eqn (4) (solid line). The error bars result from error propagation in the determination of the temperature uncertainty by eqn (3) and the shadowed area marks the error in the temperature uncertainty using eqn (4) (ESI)†.

of our knowledge, the highest reported (by one order of magnitude) for the physiological range for luminescent Nd^{3+} -based thermometers (Table 1). As the emission spectra of $(\text{Gd}_{0.991}\text{Nd}_{0.009})_2\text{O}_3$ measured with the R928 photomultiplier (Fig. 4A) were not corrected for the detector response, the calculated sensitivity values are somehow convoluted by that response. However, this correction is a multiplicative factor affecting essentially I_2 and, thus, we should not anticipate significant changes on the S_r values. Furthermore, the total integration of the ${}^4\text{F}_{3/2} \rightarrow {}^4\text{I}_{9/2}$ transition (I_2) cannot be acquired completely, which in turn limits the possibility of correlating the measured thermal sensitivity with the Boltzmann statistics for temperature-induced population distribution.

Moreover, the reported maximum S_r value is one of the highest value reported so far for nanothermometers operating in the first transparent near infrared window at temperatures in the physiological range.²⁶ For instance, the value presented here is comparable with the maximum S_r value of $\text{CaF}_2:\text{Tm}^{3+}$, Yb^{3+} nanoparticles, around $2\% \text{ K}^{-1}$ at 299 K.³⁶ We should emphasize, however, that the comparison presented in Fig. 4 of ref. 26 mix relative with absolute thermal sensitivity values (for instance the value reported for $\text{Y}_2\text{O}_3:\text{Tm}^{3+}, \text{Yb}^{3+}$ nanoparticles³⁷ is the absolute sensitivity S_a). Compared to the absolute sensitivity, $S_a = \partial\Delta/\partial T$, S_r presents the critical advantage of be independent of the nature of the thermometer (*i.e.* mechanical, electrical, luminescent) allowing the direct and quantitative comparison between thermometers, a powerful tool for all applications where different techniques must be pondered.

If the relative sensitivity allows comparing the performance of different materials, the temperature uncertainty, δT , depends on the actual temperature resolvable by the material, and on the experimental detection setup:³⁸

$$\delta T = \frac{1}{S_r} \frac{\delta \Delta}{\Delta} \quad (3)$$

where $\delta\Delta/\Delta$ is the relative uncertainty in the determination of the thermometric parameter (determined by the acquisition setup). Using the error in Δ resulting from the error propagation in the determination of the integrated areas this term is estimated to be at 0.24%. Fig. 5B shows the temperature dependence of the temperature uncertainty of the $(\text{Gd}_{0.991}\text{Nd}_{0.009})_2\text{O}_3$ nanorods. The minimum temperature uncertainty is $\delta T = 0.14 \pm 0.05 \text{ K}$. This value can be improved by decreasing the signal-to-noise ratio in the acquisition of each emission spectrum, which can be achieved by using larger integration times and/or averaging consecutive measurements of the emission spectrum. It is clear that there is a compromise between lowering the temperature uncertainty and lowering the acquisition time: the longer the acquisition time the lower the temperature uncertainty. The minimum achievable temperature uncertainty is defined by the uncertainty of the experimental setup, in the order of $\delta\Delta/\Delta \sim 0.0001\%$ for the case of a laboratory-grade fluorimeter.

The temperature uncertainty can also be assessed based on the size and system-dependent properties using the spin-

boson model.³⁹ For solid-state nanoscale thermometers, the relative fluctuation in temperature is related with the number of atoms in the sample (N_A) and its Debye temperature (T_D):³⁹

$$\delta T = \left(\frac{4T}{3\sqrt{3}T_D} e^{3T_D/8T} \right) \frac{1}{\sqrt{N_A}} T. \quad (4)$$

For T_D in the range 100 to 2000 K the term in parenthesis changes between 0.9 and 1.3, meaning that the order of magnitude of the temperature uncertainty is essentially determined by $\delta T \approx T/\sqrt{N_A}$. Fig. 5B shows the temperature dependence of the temperature uncertainty calculated with eqn (4) using $N_A = (1.5 \pm 0.5) \times 10^5$ (details of the calculus described in the ESI†) and $T_D = 362$ K (ref. 40). In this case, the number of atoms in a single nanorod is sufficient to assure, in the due time, equilibrium for any state function to be measured. Despite the fact that the estimation of the temperature uncertainty of a single nanorod is about 5 times larger than the experimental value (eqn (3)), the latter interrogates not a single nanoparticle but an ensemble of nanorods in thermal contact. In fact, considering 20–30 nanorods in contact – as shown in Fig. 2A, the agreement between theoretical (0.14–0.18 K) and experimental (0.16 K) uncertainties is very good. Thus, the theoretical temperature uncertainty should be the upper limit of the experimental temperature error.

Conclusions

Cubic phase $(\text{Gd}_{1-x}\text{Nd}_x)_2\text{O}_3$ ($x = 0.009, 0.024$ and 0.049) nanorods have been successfully synthesized by a simple wet-chemistry route at mild temperature and ambient pressure. The samples were characterized by powder XRD, ICP-AES, TEM and photoluminescence spectroscopy. The performance of $(\text{Gd}_{0.991}\text{Nd}_{0.009})_2\text{O}_3$ as an intensity-based ratiometric nanothermometer was evaluated in the 288–323 K range. These nanorods exhibit the highest thermal sensitivity and temperature uncertainty reported so far ($1.75 \pm 0.04\% \text{ K}^{-1}$ and 0.14 ± 0.05 K, respectively, at 288 K) for a nanothermometer operating in the first transparent near infrared window. The sensitivity value is one order of magnitude higher than those reported for other Nd^{3+} -based nanothermometers. Moreover, this high sensitivity was achieved using a common R928 photomultiplier tube to measure the Nd^{3+} emission in the 800–920 nm range, which allowed defining the thermometric parameter as the integrated intensity ratio of the $^4\text{F}_{5/2} \rightarrow ^4\text{I}_{9/2}$ and $^4\text{F}_{3/2} \rightarrow ^4\text{I}_{9/2}$ electronic transitions, rather than the two Stark components of the $^4\text{F}_{3/2}$ multiplet. The increase by one order of magnitude in the relative sensitivity of nanothermometers operating in the first biological transparent window permits to overcome the main drawback of previous Nd^{3+} -based nanothermometers, therefore widening the scope for using Nd^{3+} ions in deep-tissue imaging and thermal sensing.

Acknowledgements

This work was developed in the scope of the project CICECO – Aveiro Institute of Materials (Ref. FCT UID/CTM /50011/2013), financed by national funds through the FCT/MEC and when applicable co-financed by FEDER under the PT2020 Partnership Agreement. Financial support of EC Marie Curie Initial Training Network LUMINET (316906) is also acknowledged. The authors acknowledge R. A. S. Ferreira for her help with the time-resolved measurements. CDSB (SFRH/BPD/89003/2012) and MLD (SFRH/BPD/93884/2013) thank Fundação para a Ciência e Tecnologia (Portugal) for the post-doctoral grants. LDC is grateful to CAPES and CNPq (Brazil) for a fellowship within the science without borders program. FUR funding from the University of Verona is also acknowledged.

References

- 1 C. D. S. Brites, P. P. Lima, N. J. O. Silva, A. Millán, V. S. Amaral, F. Palacio and L. D. Carlos, *Nanoscale*, 2012, **4**, 4799–4829.
- 2 D. Jaque and F. Vetrone, *Nanoscale*, 2012, **4**, 4301–4326.
- 3 X. D. Wang, O. S. Wolfbeis and R. J. Meier, *Chem. Soc. Rev.*, 2013, **42**, 7834–7869.
- 4 J. Lee and N. A. Kotov, *Nano Today*, 2007, **2**, 48–51.
- 5 C. D. S. Brites, P. P. Lima, N. J. O. Silva, A. Millán, V. S. Amaral, F. Palacio and L. D. Carlos, *Adv. Mater.*, 2010, **22**, 4499–4504.
- 6 K. Okabe, N. Inada, C. Gota, Y. Harada, T. Funatsu and S. Uchiyama, *Nat. Commun.*, 2012, **3**, 705.
- 7 G. Kucsko, P. C. Maurer, N. Y. Yao, M. Kubo, H. J. Noh, P. K. Lo, H. Park and M. D. Lukin, *Nature*, 2013, **500**, 54–58.
- 8 D. Jaque, B. del Rosal, E. M. Rodriguez, L. M. Maestro, P. Haro-Gonzalez and J. G. Solé, *Nanomedicine*, 2014, **9**, 1047–1062.
- 9 M. Mecklenburg, W. A. Hubbard, E. R. White, R. Dhall, S. B. Cronin, S. Aloni and B. C. Regan, *Science*, 2015, **347**, 629–632.
- 10 A. Wickberg, J. B. Mueller, Y. J. Mange, J. Fischer, T. Nann and M. Wegener, *Appl. Phys. Lett.*, 2015, **106**, 133103.
- 11 E. J. McLaurin, L. R. Bradshaw and D. R. Gamelin, *Chem. Mater.*, 2013, **25**, 1283–1292.
- 12 J. Feng, K. J. Tian, D. H. Hu, S. Q. Wang, S. Y. Li, Y. Zeng, Y. Li and G. Q. Yang, *Angew. Chem., Int. Ed.*, 2011, **50**, 8072–8076.
- 13 L. Sambe, V. R. de La Rosa, K. Belal, F. Stoffelbach, J. Lyskawa, F. Delattre, M. Bria, G. Cooke, R. Hoogenboom and P. Woisel, *Angew. Chem., Int. Ed.*, 2014, **53**, 5044–5048.
- 14 S. L. Shinde and K. K. Nanda, *Angew. Chem., Int. Ed.*, 2013, **52**, 11325–11328.
- 15 L. H. Fischer, G. S. Harms and O. S. Wolfbeis, *Angew. Chem., Int. Ed.*, 2011, **50**, 4546–4551.
- 16 M. L. Debasu, D. Ananias, I. Pastoriza-Santos, L. M. Liz-Marzán, J. Rocha and L. D. Carlos, *Adv. Mater.*, 2013, **25**, 4868–4874.

- 17 R. Piñol, C. D. Brites, R. Bustamante, A. Martínez, N. J. Silva, J. L. Murillo, R. Cases, J. Carrey, C. Estepa, C. Sosa, F. Palacio, L. D. Carlos and A. Millán, *ACS Nano*, 2015, **9**, 3134–3142.
- 18 Y. Huang, F. Rosei and F. Vetrone, *Nanoscale*, 2015, **7**, 5178–5185.
- 19 V. Lojpur, G. Nikolic and M. D. Dramicanin, *J. Appl. Phys.*, 2014, **115**, 203106.
- 20 O. A. Savchuk, P. Haro-Gonzalez, J. J. Carvajal, D. Jaque, J. Massons, M. Aguilo and F. Diaz, *Nanoscale*, 2014, **6**, 9727–9733.
- 21 E. Carrasco, B. del Rosal, F. Sanz-Rodríguez, Á. J. de la Fuente, P. H. Gonzalez, U. Rocha, K. U. Kumar, C. Jacinto, J. G. Solé and D. Jaque, *Adv. Funct. Mater.*, 2015, **25**, 615–626.
- 22 U. Rocha, C. Jacinto da Silva, W. Ferreira Silva, I. Guedes, A. Benayas, L. Martínez Maestro, M. Acosta Elias, E. Bovero, F. C. van Veggel, J. A. García Solé and D. Jaque, *ACS Nano*, 2013, **7**, 1188–1199.
- 23 U. Rocha, K. U. Kumar, C. Jacinto, J. Ramiro, A. J. Caamano, J. G. Solé and D. Jaque, *Appl. Phys. Lett.*, 2014, **104**, 053703.
- 24 D. Wawrzynczyk, A. Bednarkiewicz, M. Nyk, W. Strek and M. Samoc, *Nanoscale*, 2012, **4**, 6959–6961.
- 25 A. Benayas, B. del Rosal, A. Perez-Delgado, K. Santacruz-Gomez, D. Jaque, G. A. Hirata and F. Vetrone, *Adv. Opt. Mater.*, 2015, **3**, 687–694.
- 26 E. N. Cerón, D. H. Ortgies, B. del Rosal, F. Ren, A. Benayas, F. Vetrone, D. Ma, F. Sanz-Rodríguez, J. G. Solé, D. Jaque and E. M. Rodríguez, *Adv. Mater.*, 2015, DOI: 10.1002/adma.201501014.
- 27 G. C. Jiang, X. T. Wei, S. S. Zhou, Y. H. Chen, C. K. Duan and M. Yin, *J. Lumin.*, 2014, **152**, 156–159.
- 28 M. L. Debasu, D. Ananias, A. G. Macedo, J. Rocha and L. D. Carlos, *J. Phys. Chem. C*, 2011, **115**, 15297–15303.
- 29 J. Planelles-Aragó, E. Cordoncillo, R. A. S. Ferreira, L. D. Carlos and P. Escribano, *J. Mater. Chem.*, 2011, **21**, 1162–1170.
- 30 A. Miguel, J. Azkargorta, R. Morea, I. Iparraguirre, J. Gonzalo, J. Fernandez and R. Balda, *Opt. Express*, 2013, **21**, 9298–9307.
- 31 N. Jaba, A. Kanoun, H. Mejri, H. Maaref and A. Brenier, *J. Phys.: Condens. Matter*, 2000, **12**, 7303–7309.
- 32 A. Benayas, D. Jaque, J. Garcia Solé, N. I. Leonyuk, E. Bovero, E. Cavalli and M. Bettinelli, *J. Phys.: Condens. Matter*, 2007, **19**, 246204.
- 33 L. D. Merkle, M. Dubinskii, K. L. Schepler and S. M. Hegde, *Opt. Express*, 2006, **14**, 3893–3905.
- 34 W. T. Carnall, H. Crosswhite and H. M. Crosswhite, *Energy level structure and transition probabilities in the spectra of the trivalent lanthanides in LaF₃*, Argonne Nat. Lab. 78-XX-95 Rep., 1977.
- 35 V. K. Rai, *Appl. Phys. B: Lasers Opt.*, 2007, **88**, 297–303.
- 36 N. N. Dong, M. Pedroni, F. Piccinelli, G. Conti, A. Sbarbati, J. E. Ramírez-Hernández, L. M. Maestro, M. C. Iglesias de la Cruz, F. Sanz-Rodríguez, A. Juarranz, F. Chen, F. Vetrone, J. A. Capobianco, J. G. Solé, M. Bettinelli, D. Jaque and A. Speghini, *ACS Nano*, 2011, **5**, 8665–8671.
- 37 V. Lojpur, M. Nikolic, L. Mancic, O. Milosevic and M. D. Dramicanin, *Ceram. Int.*, 2013, **39**, 1129–1134.
- 38 Z. P. Wang, D. Ananias, A. Carne-Sanchez, C. D. S. Brites, I. Imaz, D. MasPOCH, J. Rocha and L. D. Carlos, *Adv. Funct. Mater.*, 2015, **25**, 2824–2830.
- 39 R. Alicki and D. M. Leitner, *J. Phys. Chem. B*, 2015, DOI: 10.1021/jp508047q.
- 40 J. A. Haglund and O. Hunter, *J. Am. Ceram. Soc.*, 1973, **56**, 327–330.
- 41 J. F. Wyart, A. Meftah, A. Bachelier, J. Sinzelle, W. U. L. Tchang-Brillet, N. Champion, N. Spector and J. Sugar, *J. Phys. B: At., Mol. Opt. Phys.*, 2006, **39**, L77–L82.
- 42 X. Tian, X. Wei, Y. Chen, C. Duan and M. Yin, *Opt. Express*, 2014, **22**, 30333–30345.
- 43 W. Xu, Q. Song, L. Zheng, Z. Zhang and W. Cao, *Opt. Lett.*, 2014, **39**, 4635–4638.